Republic of Iraq.

Ministry of Higher Education And Scientific Research.

University of Babylon.

College of Education for pure Sciences.

Some Mathematical Applications in Medicine

Research Submitted to university of Babylon / college of Education for pure Sciences / Mathematic Department as part of The Requirements for the Degree of B.Sc. in mathematical science.

By

Reyam Ayad Jaber

Supervised By

Prof.Dr. Ahmed Abed Ali

1445/1444   **2024/2023**

بِسْمِ اللَّهِ الرَّحْمَنِ الرَّحِيمِ

﴿رَبِّ اشْرَحْ لِي صَدْرِي ﴿٢٥﴾ وَيَسِّرْ لِي أَمْرِي ﴿٢٦﴾ وَاحْلُلْ عُقْدَةً مِّن لِّسَانِي ﴿٢٧﴾ يَفْقَهُوا قَوْلِي ﴿٢٨﴾﴾

(سورة طه/ الأية ٢٥ ــ ٢٨)

الاهداء

إلى من لولا وجوده لساخت الأرض بأهلها وهلك الناس ...

إلى من هو كالمطر الذي يُحيي الأرض بعد موتها ...

الى من قال فيه رسول الله «ص» إي والذي بعثني بالنبوة إنهم لينتفعون به و
يستضيئون بنور ولايته في غيبته كأنتفاع الناس بالشمس وإن جللها السحاب
...

إلى الامام لمهدي المنتظر، عجل الله فرجه الشريف ...

أرجو من الله تعالى أن يتقبل مني هذا العمل المتواضع، وأن يجعله خالصاً
لوجهه الكريم .....

مع خالص الدعاء والاحترام

الشكر و التقدير

Examining Committee Certification

We certify that we have read the research entitled **" Some Mathematical Applications in Medicine "** by**" Reyam Ayad Jaber "** and as a committee examined the student in its contents and, according to our opinion, it is accepted as a research for the degree of B.Sc. in Education / Mathematics.

Signature:

Name: Ihsan Abed Alrahman Alwan Yaseen

Title: Asst.Lec.

Date: /   / 2024

 Member

Signature:

Name: Sanaa Kadum

Title: Asst.Lec.

Date: /   / 2024

 Member

Signature:

Name: Sarah Hussein Abeb Ali

Title: Asst.Lec.

 Date: /   / 2024

  Member

 Signature:

 Name: Ahmed Abed

Title: Prof. Dr.

 Date: /   / 2024

 Member / Advisor

Abstract

In this research, the importance of mathematics in medicine are presented. Many tools of mathematics are uses such as the subject of matrices, as well as triangular angles, including 180°, 30°, and 45°, in operating the CT and Magnetic Resonance Imaging (MRI) machine. Additionally, give an example of a person suffering from headaches and wanted to know how an MRI machine works by using matrices. Furthermore, another mathematical topic is discussed which is differential equations in the detection and treatment of early atherosclerosis. In it, we converted symptoms and treatments into differential equations and solved them. Also, Alzheimer's disease (AD) is discussed and it is a progressive neurodegenerative disease that destroys memory and cognitive skills. Many characteristics of this disease have been identified such as: how to use of mathematical modeling in the treatment of Alzheimer's disease ?, Fractal feature extraction, Concept of deep convolutional neural network, Support vector machine, and Performance analysis. Finally, the important results are discussed for Data collection, Feature extraction using the fractal model, Implementation of classification using SVM kernels, and Implementation of classification using DCNN.

Introduction

Archibald Pitcairn can be considered the forgotten father of sports medicine. He was born in Edinburgh in 1652, and died 300 years ago on October 21, 1713. He developed the theory of medical mathematics (medicine and mathematics). Although he had medical training, Pitcairn had a strong appreciation for numbers that motivated the great mathematicians of his day, including David Gregory (1659-1708).[1]

Pitcairn would build on the analytical school of therapeutic mechanics that had been supported by prominent Italian figures, including Giovanni Alfonso Borelli (1608–1679), Lorenzo Bellini (1643–1704), and Galileo Galilei (1564–1642), who in turn were inspired by Renaissance ideas. Geniuses like Leonardo da Vinci (1452-1519).[2][3]

One possible turning point in Pitcairn's application of advanced mathematical principles to the human body could be his documented interaction with Isaac Newton (1642-1727)[1] and his mathematical treatise Philosophiæ Naturalis Principia Mathematica. Soon after Pitcairn was promoted to professor of medicine at Leiden, where he formalized the concept of therapeutic mathematics in his early lectures in 1693.

In 1920, The Lancet published an article on medical mathematics [4]that stated that "the convergence between medicine and mathematics is incomplete" and that this "will eventually become a powerful alliance." While the term medical mathematics has been neglected and its use associated with pseudoscience, its original purpose has remained strong. The growing relationship between

medicine and mathematics has revolutionized healthcare to improve the lives of countless people. This year saw two Nobel Prizes awarded for their work in mathematical and experimental modeling, and continued dialogue between these simultaneously advanced fields is likely to foster future therapeutic innovations. In this research, we will present the importance of mathematics in medicine in two chapters. The first chapter will talk about the importance of mathematics, especially the subject of matrices, as well as triangular angles, including 180°, 30°, and 45°, in operating the CT and MRI machine. We also touched on a real example of a person suffering from headaches and wanted to know how an MRI machine works, so the doctor explained to him how the device works using matrices. In the second chapter, we discussed another mathematical topic, which is differential equations in the detection and treatment of early atherosclerosis. In it, we converted symptoms and treatments into differential equations and solved them. In the third chapter, Alzheimer disease (AD) is discussed where it is a progressive neurodegenerative disease that destroys memory and cognitive skills. Many characteristics of this disease have been identified such as: who to use of mathematical modeling in the treatment of Alzheimer's disease, fractal feature extraction, concept of deep convolutional neural network, support vector machine, and performance analysis. Finally, the important results are been discussed for data collection, feature extraction using the fractal model, implementation of classification using SVM kernels, and implementation of classification using DCNN.

Contents

Chapter One

1.1 Introduction

It was first studied by Johann Radon in 1917. (Radon is also famous for some very important discoveries related to the branch of mathematics called measure theory, which is the basis of integration).[6] In this chapter we discussed, how the X-ray MRI machine works using mathematics, especially matrices and trigonometric angles. We also mentioned a real-life example of a person suffering from headaches who wanted to know how an MRI machine works, and the doctor explained to him how the device works using matrices.

1.1.1 The Mathematics Of MRI (Magnitic Resonance Imaging) And CT Scans

Until relatively recently, if you had something wrong with your insides, you had to be operated on to find out what it was. Any such operation carried a significant risk, especially in the case of problems with the brain.

However, this is no longer the case; as we described in the introduction, doctors are able to use a whole variety of scanning techniques to look inside you in a completely safe say. A modern Computerized Axial Tomography (CAT) scanner is illustrated on the left. As in the figure (1.1)[6].

Figure (1.1) Modern CT scanner from siemens

In this scanner the patient lies on a bed and passes through the hole in the middle of the device. This hole contains an X-ray source which rotates around the patient. The X-rays from this source pass through the patient and are detected on the other side. The level of intensity of the X-ray can be measured accurately and the results processed. The resulting fan of X-rays is illustrated in the following figure(1.2) The level of intensity of the X-ray
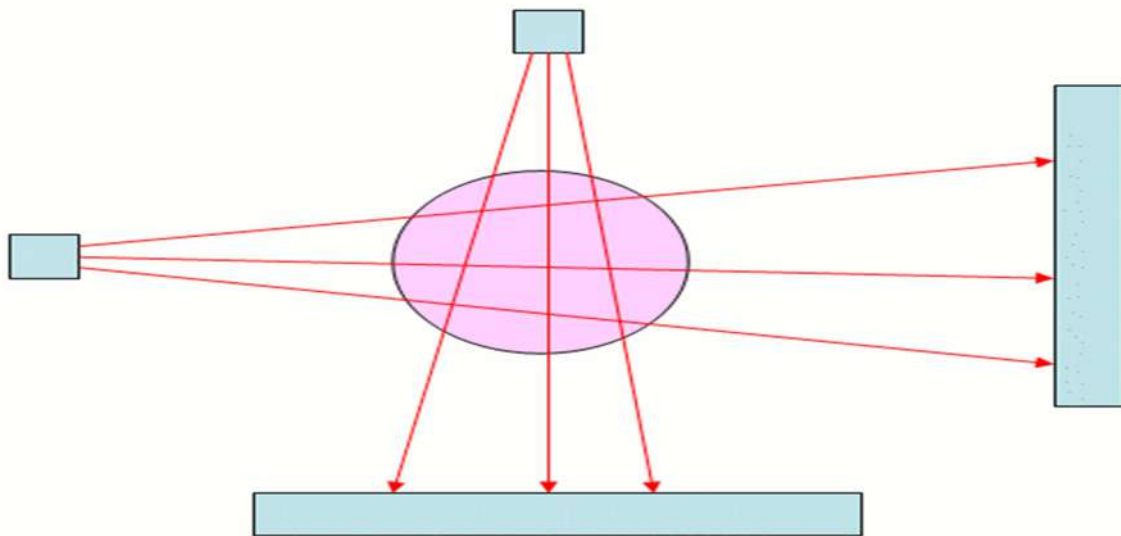
Figure (1.2) The level of intensity of the X-ray

As an X-ray passes through a patient, it is attenuated so that its intensity is reduced. The degree to which this happens depends upon what material the ray passes through: its intensity is reduced more when passing through bone than when passing through muscle, an internal organ, or a tumors. A key step in reconstructing an image of the body from a set of X-ray measurements is to carefully measure exactly how different materials absorb X-rays.[6]

When an X-ray passes through a body, it does so in a straight line, and its total absorption is a combination of the amounts to which it is absorbed by the different materials that it passes through. To see how this happens, we need to use a little calculus. Imagine that the X-ray moves along a straight line and that at a distance x into the body it has an intensity $I(x)$. As x increases, so $I(x)$ decreases as the X-ray is absorbed.[6] Now, if the X-ray travels a small distance dx, its intensity is reduced by a small amount dI. This reduction depends both on the intensity of the X-ray and the optical density $f(x)$ of the material.

Provided that the distance travelled is small enough, the reduction in intensity is related to the optical density by the formula[11]

Beer's law: $dI = -f(x)I(x)dx$

Where $f(x) -$ attenuation cofficent at x E.q(1.1)

$$\frac{dI(x)}{dx} - f(x)I(x) \Rightarrow \frac{d\ln I(x)}{dx} = -f(x) \Rightarrow e^{-\int f(x)dx} I_0$$

Now, when the X-ray enters the body it will have intensity I_{start} and when it leaves it will have intensity I_{finish}.[11] We can combine all of the contributions to the reduction in the intensity of the X-ray given by all of the parts of the body that it travels through. Doing this, we find that the attenuation (the reduction in the intensity) is given by[6]

$$I_{finish} = I_{start} e^{-R}$$ Eq.(1.2)

where

$$R = \int f(x)d$$ Eq.(1.3)

This is the attenuation of one X-ray and it gives some information about the body. Below we see in figure (1.3) an object irradiated by several X-rays with the intensity of the rays measured on a detector. Here some X-rays pass through all of the object and are strongly absorbed so that their intensity (recorded at the Center of the detector) is low, while others pass through less of the object and are less strongly absorbed. Effectively the object casts a shadow of the X-rays and from this we can work out its basic dimensions. We illustrate in figure (1.3).[6]
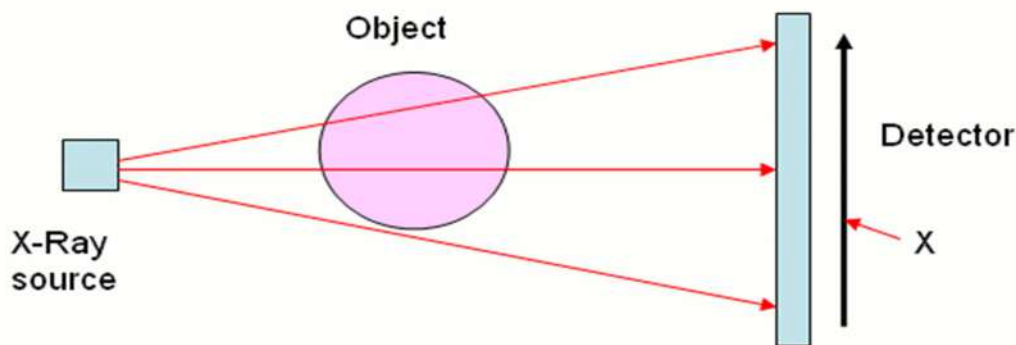

Figure (1.3) Know your basic body dimensions

We note in the figure (1.3) that it. The intensity of the X-ray where it hits the detector depends on the width of object and the length of the path travelled both through the object and the air.[6]

However, the secret to computerized axial tomography is to find out much more about the nature of the object than just its dimensions, by looking at the attenuation of as many X-rays as possible. To do this, we need to think of a number of X-rays at different angles θ and distances ρ from the center of the object. A typical such X-ray is in the figure (1.4).[6]
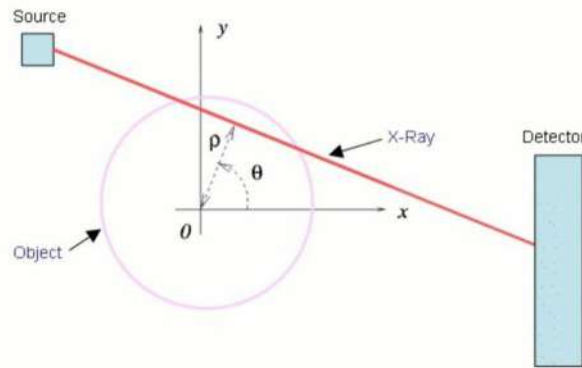

Figure (1.4) P: Distance from the object center. θ: Angle of the X-Ray.

This X-ray will pass through a series of points (x, y) at which the optical density is $u(x, y)$. Using the equation for a straight line these points are given by

$$(x, y) = (\rho \cos(\theta) - s \sin(\theta), \rho \sin(\theta) + s \cos(\theta)) \qquad \text{Eq.(1.4)}$$

where s is the distance along the X-ray. In this case we now have

$$I_{finish} = I_{start} e^{-R(\rho,\theta)} \qquad \text{Eq.(1.5)}$$

where

$$R(\rho, \theta) = \int u(\rho \cos(\theta) - s \sin(\theta), \rho \sin(\theta) + s \cos(\theta)) ds \qquad \text{Eq.(1.6)}$$

The function $R(\rho, \theta)$ is called the Radon transform of the function $u(x, y)$. The larger R is, the more an X-ray of this particular orientation is absorbed. This transformation lies at the heart of the CAT scanners and all problems in tomography By measuring the attenuation of the X-rays from as many angles as possible, it is possible to measure this function to a high accuracy.[6]

There are different types of X-rays, including MRI..

Cone-beam geomertry

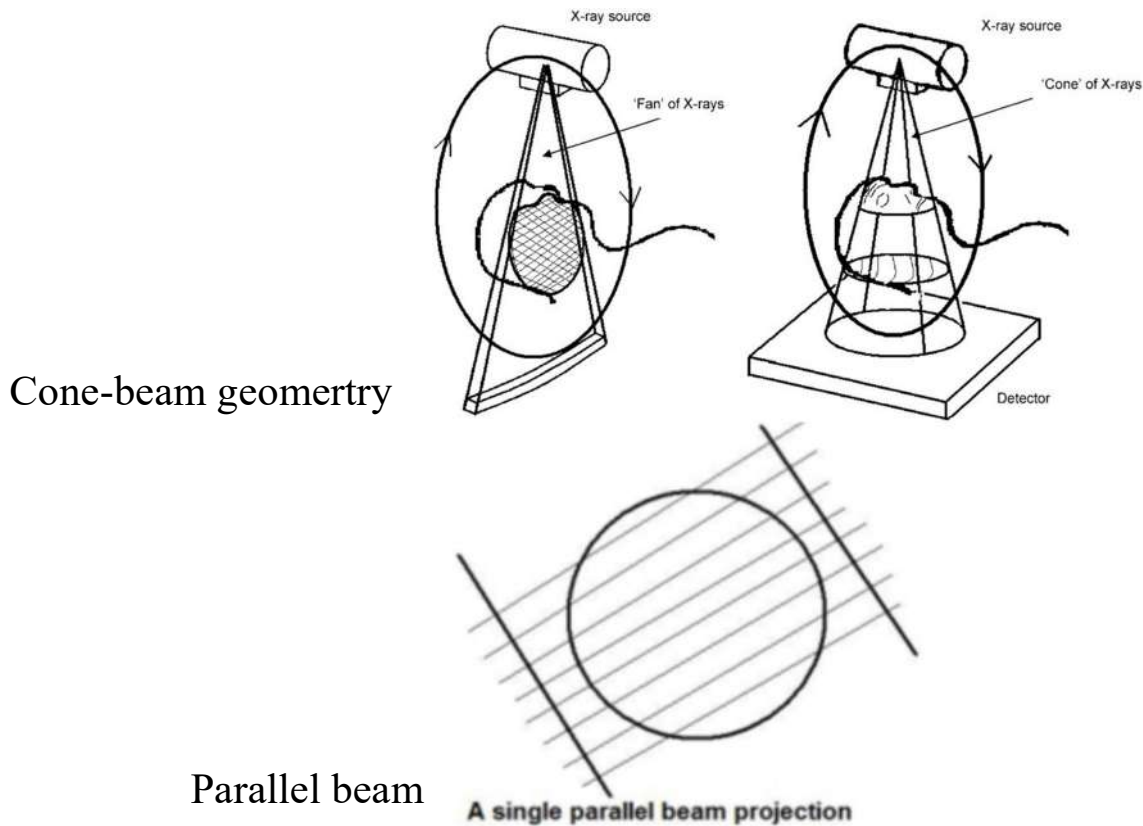Parallel beam

A single parallel beam projection

Figure (1.5) Types of X-ray shapes for the CAT

We can express the sigmoid rays of magnetic resonance by any linear to solving $A_i X_i = Y_i$ with a large diagonal matrix A:[11]

$$
\begin{pmatrix}
a_1 & 0 & 0 & \cdots & 0 \\
0 & a_2 & 0 & \cdots & 0 \\
0 & 0 & a_3 & 0 & \cdots \\
\cdots & \cdots & \cdots & \cdots & \cdots
\end{pmatrix}
\begin{pmatrix}
x_1 \\
x_2 \\
x_3 \\
\cdots
\end{pmatrix}
=
\begin{pmatrix}
y_1 \\
y_2 \\
y_3 \\
\cdots
\end{pmatrix}
$$

When a_k => 0 fast – instability.[11]

1.1.2 Example:

Noseman is having a headache and as an old-school hypochondriac he goes to see his doctor. His doctor is quite worried and makes an appointment with a radiologist for man to get a CT scan.

Because noseman always wants to know how things work he asks the radiologist about the inner workings of a CT scanner.

The basic idea is that X-rays are fired from one side of the scanner to the other. Because different sorts of tissue (like bones, brain cells, cartilage etc.) block different amounts of the X-rays the intensity measured on the other side varies accordingly.[7]

The problem is of course that a single picture cannot give the full details of what is inside the body because it is a combination of different sorts of tissue in the way of the respective X-rays. The solution is to rotate the scanner and combine the different slices.

How, you ask? Good old linear algebra to the rescue!

We start with the initial position and fire X-rays with an intensity of 30 (just a number for illustrative purposes) through the body[7]:
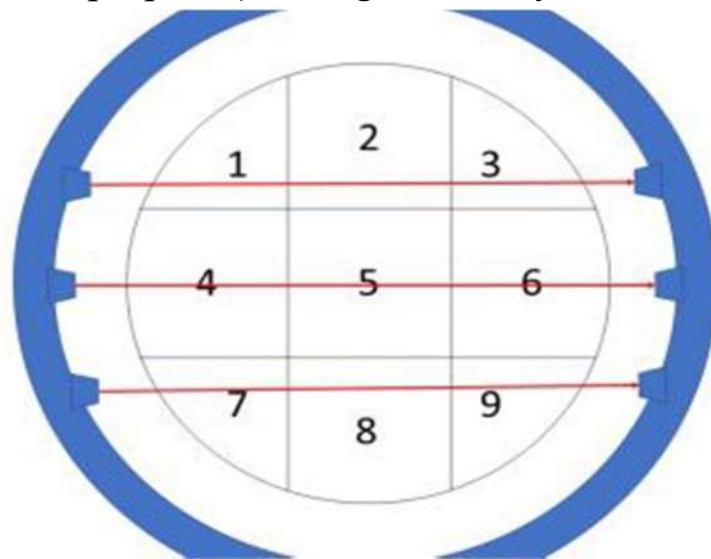

Figure (1.6) Initial position ($\theta = \pi$)

As can be seen in the picture the upper ray goes through areas 1, 2 and 3 and let's say that the intensity value of 12 is measured on the other side of the scanner:

$$30 - x1 - x2 - x3 = 12$$

Or

$$x1 + x2 + x3 = 18$$

The rest of the formula is found accordingly:

$$\underbrace{\begin{pmatrix} 1 & 1 & 1 & 0 & 0 & 0 & 0 & 0 & 0 \\ 0 & 0 & 0 & 1 & 1 & 1 & 0 & 0 & 0 \\ 0 & 0 & 0 & 0 & 0 & 0 & 1 & 1 & 1 \end{pmatrix}}_{A_1} \underbrace{\begin{pmatrix} x_1 \\ x_2 \\ x_3 \\ x_4 \\ x_5 \\ x_6 \\ x_7 \\ x_8 \\ x_9 \end{pmatrix}}_{x} = \underbrace{\begin{pmatrix} 18 \\ 21 \\ 18 \end{pmatrix}}_{b_1}$$

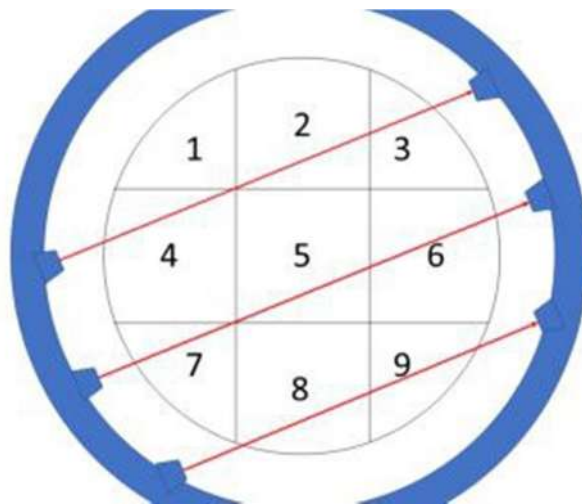Eq.(1.7)

We then rotate the scanner for the first time[7]…

Figure (1.7) Position after first rotation $(\theta 30 = \frac{\pi}{6})$

…which gives the following formula:

$$\underbrace{\begin{pmatrix} 0 & 1 & 1 & 1 & 0 & 0 & 0 & 0 & 0 \\ 0 & 0 & 0 & 0 & 1 & 1 & 1 & 0 & 0 \\ 0 & 0 & 0 & 0 & 0 & 0 & 0 & 1 & 1 \end{pmatrix}}_{A_2} \underbrace{\begin{pmatrix} x_1 \\ x_2 \\ x_3 \\ x_4 \\ x_5 \\ x_6 \\ x_7 \\ x_8 \\ x_9 \end{pmatrix}}_{x} = \underbrace{\begin{pmatrix} 18 \\ 21 \\ 9 \end{pmatrix}}_{b_2}$$
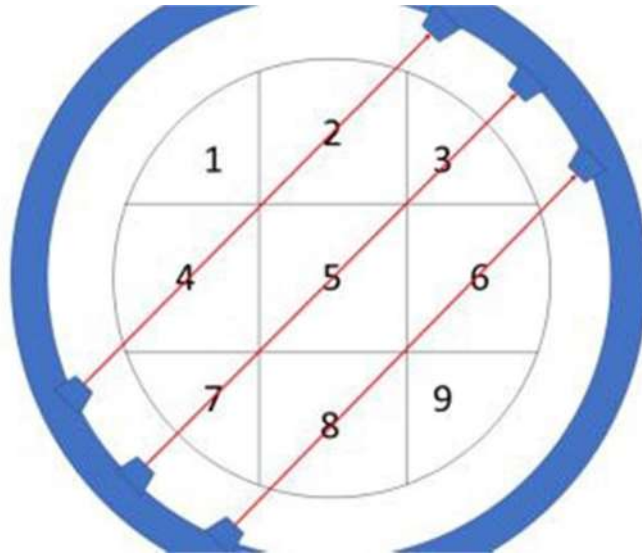
Eq.(1.8)

And a second rotation[7]…

Figure (1.8) Position after second rotaition ($\theta 45 = \pi/4$)

…yields the following formula:

$$\underbrace{\begin{pmatrix} 0 & 1 & 0 & 1 & 0 & 0 & 0 & 0 & 0 \\ 0 & 0 & 1 & 0 & 1 & 0 & 1 & 0 & 0 \\ 0 & 0 & 0 & 0 & 0 & 1 & 0 & 1 & 0 \end{pmatrix}}_{A_3} \underbrace{\begin{pmatrix} x_1 \\ x_2 \\ x_3 \\ x_4 \\ x_5 \\ x_6 \\ x_7 \\ x_8 \\ x_9 \end{pmatrix}}_{x} = \underbrace{\begin{pmatrix} 18 \\ 14 \\ 16 \end{pmatrix}}_{b_3} \qquad \text{Eq.(1.9)}$$

Now we are combining all three systems of equations:

$$\begin{pmatrix} A_1 \\ A_2 \\ A_3 \end{pmatrix} x = \begin{pmatrix} b_1 \\ b_2 \\ b_3 \end{pmatrix} \qquad \text{Eq.(1.10)}$$

14

or written out in full:

$$\begin{pmatrix} 1 & 1 & 1 & 0 & 0 & 0 & 0 & 0 & 0 \\ 0 & 0 & 0 & 1 & 1 & 1 & 0 & 0 & 0 \\ 0 & 0 & 0 & 0 & 0 & 0 & 1 & 1 & 1 \\ 0 & 1 & 0 & 1 & 0 & 0 & 0 & 0 & 0 \\ 0 & 0 & 1 & 0 & 1 & 0 & 1 & 0 & 0 \\ 0 & 0 & 0 & 0 & 0 & 1 & 0 & 1 & 0 \\ 0 & 1 & 0 & 1 & 0 & 0 & 0 & 0 & 0 \\ 0 & 0 & 1 & 0 & 1 & 0 & 1 & 0 & 0 \\ 0 & 0 & 0 & 0 & 0 & 1 & 0 & 1 & 0 \end{pmatrix} \begin{pmatrix} x_1 \\ x_2 \\ x_3 \\ x_4 \\ x_5 \\ x_6 \\ x_7 \\ x_8 \\ x_9 \end{pmatrix} = \begin{pmatrix} 18 \\ 21 \\ 18 \\ 18 \\ 21 \\ 9 \\ 18 \\ 14 \\ 16 \end{pmatrix}$$

$$\underbrace{}_{\mathbf{A}} \quad \underbrace{}_{\mathbf{x}} \quad \underbrace{}_{\mathbf{b}}$$

Eq.(1.11)

Here is the data of the matrix A for you to download: ct-scan.txt.

We now have 9 equations with 9 unknown variables… which should easily be solvable by R, which can also depict the solution as a gray-scaled image… the actual CT-scan![7]

A <- read.csv("data/ct-scan.txt")

b <- c(18, 21, 18, 18, 21, 9, 18, 14, 16)

v <- solve (A, b)

matrix(v, ncol = 3   ,   byrow = TRUE)

[,1] [,2] [,3]

[1,]   9   9   0

[2,]   9   5   7

[3,]   9   9   0

Image (matrix (v, ncol = 3), col = gray (4:0 / 4))
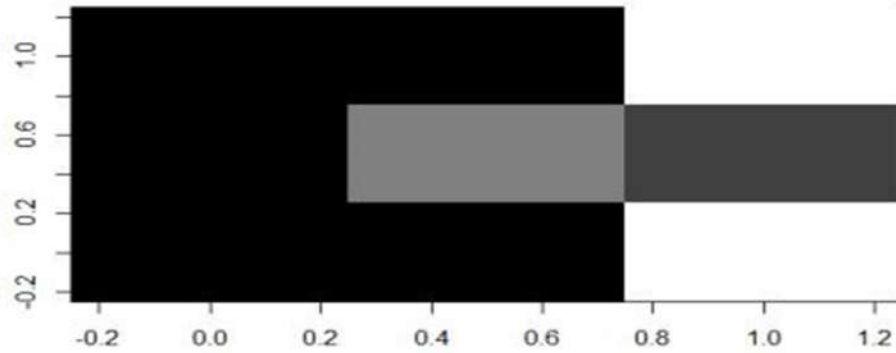
Figure (1.9) CT of Noseman

The radiologist looks at the picture… and has good news for Noseman: everything is how it should be! Noseman is relieved and his headache is much better now…

Real CT scans make use of the same basic principles (of course with a lot of additional engineering and maths magic).[7]

Here are real images of CT scans of a human brain…

Figure (1.10) Real images of CT Scans of a human brain.

… which can be combined into a 3D-animation:

Figure (1.11) 3D-animation of real images of ct scans of a human brain.

Isn't it fascinating how a little bit of maths can save lives![7]

1.2 Conclusion

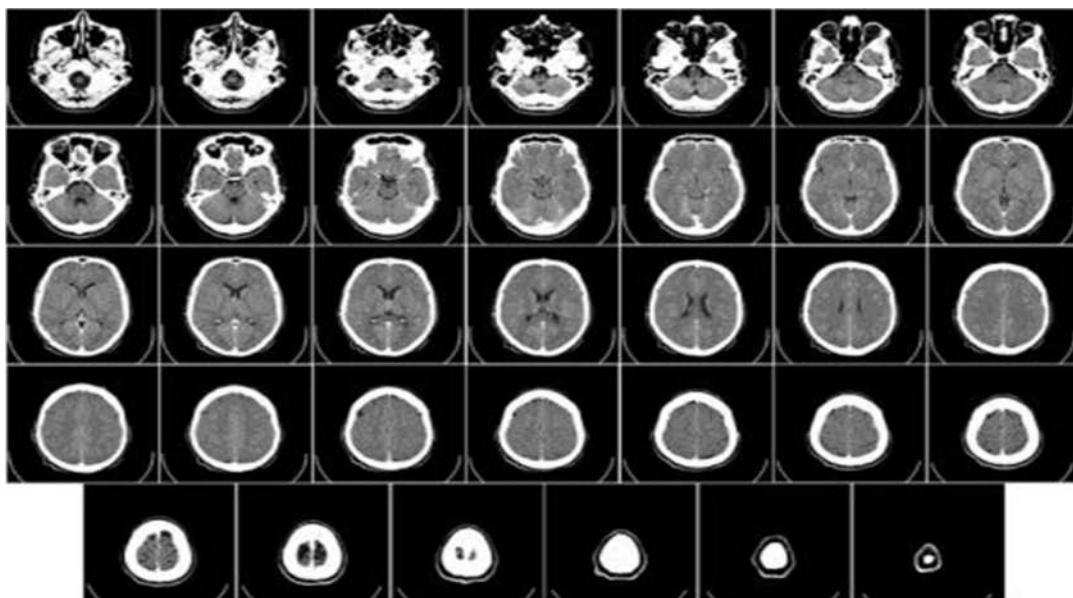Magnetic resonance imaging (MRI) is used to reduce surgical procedures and diagnose a patient's condition more accurately than other devices. It minimizes significant risks, especially in cases of brain problems, in a completely safe manner. The first to study this research was the scientist Johann Radon. The importance of using mathematics in MRI lies in directing X-rays at an angle that results in less absorption by the body and greater penetration. We used Beer's law,

Beer's law: $dI = -f(x)I(x)dx$

 and its benefit is to reduce the intensity of the X-rays passing through parts of the body (because an increase in X-rays can cause cancerous diseases). For example, Nozeman, who suffered from headaches and also had hypochondria, underwent some tests by the doctor using MRI to diagnose his condition more accurately and provide more than one angle (180, 30, and 45 degrees) to give full details inside the body because it is a mixture of different types of tissues. We used matrices to express the passage of X-rays through the patient, and the matrices were solved through tomography to display the results of the MRI."

Chapter Two

2.1Introduction

In this chapter Atherosclerosis is a chronic disease which involves the build up of cholesterol and fatty deposits within the inner lining of the artery. It is associated with a progressive thickening and hardening of the arterial wall that result in narrowing of the vessel lumen and restriction of blood flow to vital organs. These events may cause heart attack or stroke, the commonest causes of death worldwide. In this paper we study the early stages of atherosclerosis via a mathematical model of partial differential equations of reaction-diffusion type.[8]

2.1.1 Mathematical modeling of inflammatory processes of atherosclerosis

Figure (2.1) MATHEMATICAL MODELLING OF CARDIOVASCULAR SYSTEM
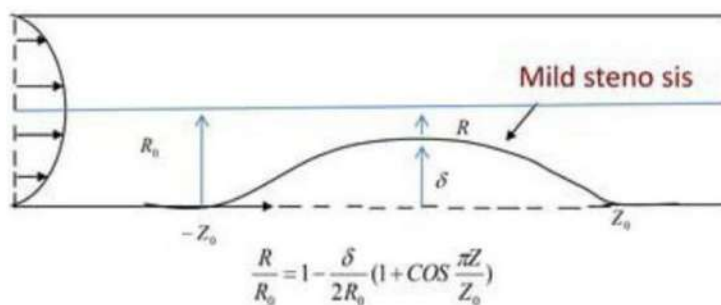

$$\frac{R}{R_0} = 1 - \frac{\delta}{2R_0}(1 + COS\frac{\pi Z}{Z_0})$$

Figure (2.2) Sketch of flow of fluid with mild stenosis in one wall steady poiseuille flow.

Radius of tube is larger than stenosis $\quad \delta/R_0 <<1$

2.1.2 Mathematical model

TABLE 1. Notations description.

L	Concentration of LDL
H	Concentration of HDL
L_{ox}	Concentration of ox-LDL
A_1	Concentration of pro-inflammatory monocytes
A_2	Concentration of anti-inflammatory monocytes
M_1	Concentration of pro-inflammatory (M1) macrophages
M_2	Concentration of anti-inflammatory (M2) macrophages
T_1	Concentration of Th1
T_2	Concentration of Th2
C_1	Concentration of Th1 cytokines
C_2	Concentration of Th2 cytokines
C_3	Concentration of pro-inflammatory cytokines produced by M1 macrophages
C_4	Concentration of anti-inflammatory cytokines produced by M2 macrophages
F	Concentration of foam cells

In this section, we model the different cascades of atherogenesis in a system of coupled partial differential equations. We consider some key-role. players in the inflammatory process shown in Table 1. The endothelial dysfunction and activation are taken into consideration through a term P considered to be an endothelial permeability indicator. The modeling of the term P can involve the effect of ox-LDL and free radicals in endothelial dysfunction, the effect of pro-inflammatory cytokines in endothelial activation, the effect of HDL in preserving endothelium and finally, the effect of nitric oxide or shear stress.

For $l > 0$, $x \in]0, l[$ and $t \in [0, \infty]$, the system reads as follows:

The following equation models the evolution of LDL concentration:

$$\frac{\partial H}{\partial t} = D_2 \frac{\partial^2}{\partial x^2} + \sigma_H\, PH_a - k_H H \qquad\qquad \text{Eq. (2.1)}$$

The first right-hand side term in equation represents the diffusion of LDL and the second right-hand side term describes the LDL penetration through the vessel wall, where L0 is the concentration of LDL in the blood. The third right-hand side term describes the oxidization of LDL particles.

In subsequent equations, the terms Di, for i = 2, ..., 14, refer to the diffusion rates. Similar reactions are modeled for the HDL concentration as follows:

$$\frac{\partial L}{\partial t} = D_1 \frac{\partial^2 L}{\partial x^2} + \sigma_L PL_0 - k_L L \qquad\qquad \text{Eq. (2.2)}$$

The HDL penetration through the vessel wall is described through the second right-hand side term in equation, where H0 is the concentration of HDL in the

21

blood. The consumption of HDL through oxidation reaction with free radicals is represented in the third right-hand side term.[8]

The evolution of ox-LDL concentration in the intima is modeled by the following equation:

$$\frac{\partial L_{ox}}{\partial t} = D_3 \frac{\partial^2 L_{ox}}{\partial x^2} + k_L L - \lambda_{L_{ox}} M_1 \frac{L_{ox}}{k_{L_{ox}}+L_{ox}} M_1 - \lambda_{L_{ox}} M_2 \frac{L_{ox}}{k_{L_{ox}}+L_{ox}} M_2 - d_{L_{ox}} L_{ox} \quad \text{Eq.(2.3)}$$

We model the production of ox-LDL due to LDL oxidation by reaction with the radicals through the term kLL in equation, and the ingestion of ox-LDL by M1 and M2 macrophages through the third and fourth right-hand side terms. The last term models the degradation of ox-LDL.

The description of monocytes concentrations evolution is given by:

$$\frac{\partial A_1}{\partial t} = D_4 \frac{\partial^2 A_1}{\partial x^2} + \lambda_{PA_1} PA_1^0 - \lambda_{C_1 A_1} \frac{C_1}{k_{C_1}+C_1+k_4 C_4} A_1 - d_{A_1} A_1 \qquad \text{Eq.(2.4)}$$

$$\frac{\partial A_2}{\partial t} = D_5 \frac{\partial^2 A_2}{\partial x^2} + \lambda_{PA_2} PA_2^0 - \lambda C_2 A_2 \frac{C_2}{k_{C_2}+C_2} A_2 - d_{A_2} A_2 \qquad \text{Eq.(2.5)}$$

The terms $\lambda_{P\,A1}\,PA^0_{\,1}$ and $\lambda_{P\,A2}\,PA_2^{\,0}$, in equations, model the A_1 and A_2 monocytes penetration through the vessel wall, where $A_1^{\,0}$ and $A_2^{\,0}$ are densities of A_1 and A_2 monocytes in blood. The third right-hand side terms describe the differentiation of monocytes into macrophages, and the last right-hand side terms correspond to the death of monocytes.

The following equations describe the evolution of M1 and M2 macrophages concentrations:

$$\frac{\partial M_1}{\partial t} = D_6 \frac{\partial^2 M_1}{\partial x^2} + \lambda_{C_1 A_1} \frac{C_1}{k_{C_1}+C_1+K_4 C_4} A_1 - \lambda_{L_{ox}} M_1 \frac{L_{ox}}{k_{L_{ox}}+L_{ox}} M_1 - d_{M_1} M_1 \qquad \text{Eq.(2.6)}$$

$$\frac{\partial M_2}{\partial t} = D_7 \frac{\partial^2 M_2}{\partial x^2} + \lambda_{C_2 A_2} \frac{C_2}{k_{C_2}+C_2} A_2 - \lambda_{L_{ox}} M_2 \frac{L_{ox}}{k_{L_{ox}}+L_{ox}} M_2 - d_{M_2} M_2 \qquad \text{Eq.(2.7)}$$

The second right-hand side terms of equations correspond to the differentiation of monocytes into macrophages, the third right-hand side terms describe the uptake of ox-LDL by macrophages and the transformation of macrophages into foam cells, and the fourth right-hand side terms represent the death of macrophages.[8]

The intimal concentrations of T-helper cells satisfy the following equations:

$$\frac{\partial C_1}{\partial t} = D_{10}\frac{\partial^2 C_1}{\partial x^2} + \lambda_{C_1}T_1 - \lambda_{C_1 A_1}\frac{C_1}{k_{C_1} + C_1 + k_4 C_4}A_1 - d_{C_1}C_1, \qquad \text{Eq.(2.8)}$$

$$\frac{\partial C_2}{\partial t} = D_{11}\frac{\partial^2 C_2}{\partial x^2} + \lambda_{C_2}T_2 - \lambda_{C_2 A_2}\frac{C_2}{k_{C_2} + C_2}A_2 - d_{C_2}C_2. \qquad \text{Eq.(2.9)}$$

Equations model the influx of T-helper cells from the blood into the intima due to the permeability of the endothelium and the death of T-helper cells.

The concentrations of cytokines released by T-helper cells are described through the following equations:

$$\frac{\partial C_3}{\partial t} = D_{12}\frac{\partial^2 C_3}{\partial x^2} + \lambda_{C_3 M_1}\frac{C_3}{k_{C_3} + C_3 + kC_4}M_1 + \lambda_{C_4 F}\frac{1}{k_{C_4} + C_4}F - d_{C_3}C_3. \qquad \text{Eq.(2.10)}$$

$$\frac{\partial C_4}{\partial t} = D_{13}\frac{\partial^2 C_4}{\partial x^2} + \lambda_{C_4}M_2 - d_{C_4}C_4. \qquad \text{Eq.(2.11)}$$

We model the production of C_1 and C_2 cytokines by T-cells in equations and at rates of λ_{C1} and λ_{C2} . The differentiation of A_1 into M_1 macrophages (down regulated by C_4) and the differentiation of A_2 monocytes into M_2 macrophages are modeled by the third right-hand side terms. The last terms correspond to the degradation of cytokines.[8]

In the following equations, we model the evolution in time of cytokines produced by M1 and M2 macrophages:

$$\frac{\partial T_1}{\partial t} = D_8\frac{\partial^2 T_1}{\partial x^2} + \lambda_{PT_1}PT_1^0 - d_{T_1}T_1, \qquad \text{Eq.(2.12)}$$

$$\frac{\partial T_2}{\partial t} = D_9\frac{\partial^2 T_2}{\partial x^2} + \lambda_{PT_2}PT_2^0 - d_{T_2}T_2. \qquad \text{Eq.(2.13)}$$

The production of anti-inflammatory cytokines C_4 by M_2 macrophages is described by the second right-hand side term in equation. The third right-hand side term corresponds to the degradation of cytokines.

The evolution of foam cells concentration is modeled as follows:

$$\frac{\partial F}{\partial t} = D_{14}\frac{\partial^2 F}{\partial x^2} + \lambda_{L_{ox}M_1}\frac{L_{ox}}{k_{L_{ox}} + L_{ox}}M_1 + \lambda_{L_{ox}M_2}\frac{L_{ox}}{k_{L_{ox}} + L_{ox}}M_2 - d_F F. \qquad \text{Eq.(2.14)}$$

The second and third right-hand side terms of equation correspond to the formation of foam cells due to the ingestion of ox-LDL by M_1 and M_2 macrophages. The last term describes the death of foam cells.[8]

2.1.3 Reduced model

In this section, we consider a reduced model that originates from the complete model. In this reduced model, we particularly consider the pro-inflammatory process. Therefore, we let $H = A_2 = M_2 = T_2 = C_2 = C_4 = F = 0$. We further consider the production of Th1 cells and Th1 cytokines are compensated respectively by the loss of Th1 cells and Th1 cytokines, in an unbiased manner. For the sake of ease, we also take $d_{A1} = k_{C1} = 0$.[8]

We consider the following new notations: $\lambda_1 = \sigma_L L_0$, $\lambda_2 = \lambda_{L_{ox}M_1}$, $\lambda_3 = \lambda_{PA1}A^0_1$

, $\lambda_4 = \lambda_{C_1 A_1}$, $\lambda_5 = \lambda_{C_3 M_1}$,

$k_2 = kL_{ox}$, $k_3 = kC_3$, $d_1 = dL_{ox}$, $d_2 = dM_1$ and $d_3 = dC_3$. The reduced model becomes:

$$\frac{\partial L}{\partial t} = D_1\frac{\partial^2 L}{\partial x^2} + \lambda_1 P - k_L L, \qquad \text{Eq.(2.15)}$$

$$\frac{\partial L_{ox}}{\partial t} = D_3\frac{\partial^2 L_{ox}}{\partial x^2} + k_L L - \lambda_2\frac{L_{ox}}{k_2 + L_{ox}}M_1 - d_1 L_{ox}, \qquad \text{Eq.(2.16)}$$

$$\frac{\partial A_1}{\partial t} = D_4\frac{\partial^2 A_1}{\partial x^2} + \lambda_3 P - \lambda_4 A_1, \qquad \text{Eq.(2.17)}$$

$$\frac{\partial M_1}{\partial t} = D_6\frac{\partial^2 M_1}{\partial x^2} + \lambda_4 A_1 - \lambda_2\frac{L_{ox}}{k_2 + L_{ox}}M_1 - d_2 M_1, \qquad \text{Eq.(2.18)}$$

$$\frac{\partial C_3}{\partial t} = D_{12}\frac{\partial^2 C_3}{\partial x^2} + \lambda_5\frac{C_3}{k_3 + C_3}M_1 - d_3 C_3. \qquad \text{Eq.(2.19)}$$

$$P = H(\alpha)\frac{P_0 + L_{ox} + cC_3}{k_1 + L_{ox} + cC_3}, \qquad \text{Eq.(2.20)}$$

24

In the ensuing sections, we study this reduced model with a constant permeability indicator P, and with a variable one.[8]

2.1.4 Reduced model with variable P

In this section, we consider the term P to be a function of L_{ox} and C_3 as follows:

$$P = H(\alpha)\frac{P_0 + L_{ox} + cC_3}{k_1 + L_{ox} + cC_3},$$

Eq.(2.21)

where:

✓ α refers to the assessment of endothelial dysfunction due to external stimuli. Note that vascular function can be measured by several methods, including invasive and non-invasive techniques. α is an independant parameter that is altered upon exposure of the endothelium to cardiovascular risk factors such as low shear stress, nicotine circulating in blood and high plasma concentration of cholesterol.[8]

✓ $H(\alpha)$ describes the activation and dysfunction of the endothelium and is given by

$$H(\alpha) = \begin{cases} 0 & \text{if } \alpha < \alpha_0, \\ 1 & \text{otherwise,} \end{cases}$$

Eq.(2.22)

where α_0 represents a threshold to discriminate between normal and abnormal endothelial function. A thick glycocalyx, active endothelial cells, an appropriate endothelial production of NO and a tight chain of junctions are typical features of a normal endothelium. An endothelium in good condition is then assessed through the parameter α with $\alpha < \alpha_0$. When the glycocalyx is damaged by cardiovascular risk factors conditions, it causes a decreased production of NO, that in turn results in endothelial dysfunction and activation and tight junctions disruption. All the cascades together lead to increased endothelial permeability. Thus, it is the degradation of the glycocalyx that

initiates endothelial dysfunction. Impaired endothelial function associated with a compromised glycocalyx is detected when $\alpha > \alpha_0$

✓ The term $\frac{P0+Lox+cC3}{K1+Lox+cC3}$ describes the permeability of the endothelium, where P_0 refers to the selective permeability of a healthy endothelium, i.e. the permeability to small molecules and k_1 denotes the effect of endothelial regulators, i.e. HDL, NO and SS.[8]

We substitute the following variables $\tilde{C_3} = cC_3$, $\tilde{k_3} = ck_3$, $\tilde{\lambda_5} = c\lambda_5$ and $\tilde{D_{12}} = \frac{D12}{c}$, in equations and use P as in equation, then we drop the tildes. The new reduced system reads:

$$\frac{\partial L}{\partial t} = D_1\frac{\partial^2 L}{\partial x^2} + \lambda_1 H(\alpha)\frac{P_0 + L_{ox} + C_3}{k_1 + L_{ox} + C_3} - k_L L, \qquad \text{Eq.(2.23)}$$

$$\frac{\partial L_{ox}}{\partial t} = D_3\frac{\partial^2 L_{ox}}{\partial x^2} + k_L L - \lambda_2\frac{L_{ox}}{k_2 + L_{ox}}M_1 - d_1 L_{ox} \qquad \text{Eq.(2.24)}$$

$$\frac{\partial A_1}{\partial t} = D_4\frac{\partial^2 A_1}{\partial x^2} + \lambda_3 H(\alpha)\frac{P_0 + L_{ox} + C_3}{k_1 + L_{ox} + C_3} - \lambda_4 A_1, \qquad \text{Eq.(2.25)}$$

$$\frac{\partial M_1}{\partial t} = D_6\frac{\partial^2 M_1}{\partial x^2} + \lambda_4 A_1 - \lambda_2\frac{L_{ox}}{k_2 + L_{ox}}M_1 - d_2 M_1, \qquad \text{Eq.(2.26)}$$

$$\frac{\partial C_3}{\partial t} = D_{12}\frac{\partial^2 C_3}{\partial x^2} + \lambda_5\frac{C_3}{k_3 + C_3}M_1 - d_3 C_3. \qquad \text{Eq.(2.27)}$$

The kinetic system becomes:

$$\frac{dL}{dt} = \lambda_1 H(\alpha)\frac{P_0 + L_{ox} + C_3}{k_1 + L_{ox} + C_3} - k_L L, \qquad \text{Eq.(2.28)}$$

$$\frac{dL_{ox}}{dt} = k_L L - \lambda_2\frac{L_{ox}}{k_2 + L_{ox}}M_1 - d_1 L_{ox}, \qquad \text{Eq.(2.29)}$$

$$\frac{dM_1}{dt} = \lambda_4 A_1 - \lambda_2\frac{L_{ox}}{k_2 + L_{ox}}M_1 - d_2 M_1, \qquad \text{Eq. (2.30)}$$

$$\frac{dA_1}{dt} = \lambda_3 H(\alpha)\frac{P_0 + L_{ox} + C_3}{k_1 + L_{ox} + C_3} - \lambda_4 A_1, \qquad \text{Eq. (2.31)}$$

26

$$\frac{dC_3}{dt} = \lambda_5 \frac{C_3}{k_3 + C_3} M_1 - d_3 C_3 \qquad \text{Eq.(2.32)}$$

The Jacobian matrix of system reads:

$$J = \begin{bmatrix} -k_L & \lambda_1 H(\alpha)\dfrac{k_1 - P_0}{(k_1 + L_{ox} + C_3)^2} & 0 & 0 & \lambda_1 H(\alpha)\dfrac{k_1 - P_0}{(k_1 + L_{ox} + C_3)^2} \\ k_L & \lambda_2 \dfrac{k_2 M_1}{(k_2 + L_{ox})^2} - d_1 & 0 & -\lambda_2 \dfrac{L_{ox}}{k_2 + L_{ox}} & 0 \\ 0 & \lambda_3 H(\alpha)\dfrac{k_1 - P_0}{(k_1 + L_{ox} + C_3)^2} & -\lambda_4 & 0 & \lambda_3 H(\alpha)\dfrac{k_1 - P_0}{(k_1 + L_{ox} + C_3)^2} \\ 0 & -\lambda_2 \dfrac{k_2 M_1}{(k_2 + L_{ox})^2} & \lambda_4 & -\lambda_2 \dfrac{L_{ox}}{k_2 + L_{ox}} - d_2 & 0 \\ 0 & 0 & 0 & \lambda_5 \dfrac{C_3}{k_3 + C_3} & \lambda_5 \dfrac{k_3 M_1}{(k_3 + C_3)^2} - d_3 \end{bmatrix} . \qquad \text{Eq.(2.33)}$$

We recall that a system is said to be monotone if the off-diagonal elements of its Jacobian are non negative. To ensure the monotonicity of system, we assume that $k_1 > P_0$, and we conduct the study for $\lambda_2 = 0$, then we can extend the results for λ_2 close to zero, by applying the implicit function theorem for the existence and stability of the fixed points.[8]

For the sake of ease, we take $P_0 = 0$. Similarly, we use the implicit function theorem to conclude for P_0 in a small positive neighborhood of 0.

Therefore, finding the fixed points of system with $\lambda_2 = P_0 = 0$ amounts to solving the following system:

$$\lambda_1 H(\alpha)\frac{L_{ox} + C_3}{k_1 + L_{ox} + C_3} - d_1 L_{ox} = 0, \qquad \text{Eq.(2.34)}$$

$$\lambda_3 H(\alpha)\frac{L_{ox} + C_3}{k_1 + L_{ox} + C_3} - d_2 M_1 = 0, \qquad \text{Eq.(2.35)}$$

$$\lambda_5 \frac{C_3}{k_3 + C_3} M_1 - d_3 C_3 = 0, \qquad \text{Eq.(2.36)}$$

$$L = \frac{\lambda_1}{k_L} H(\alpha)\frac{L_{ox} + C_3}{k_1 + L_{ox} + C_3}, \qquad \text{Eq.(2.37)}$$

$$A_1 = \frac{\lambda_3}{\lambda_4} H(\alpha) \frac{L_{ox} + C_3}{k_1 + L_{ox} + C_3}.$$ Eq.(2.38)

Since the unknowns of system represent concentrations of physical quantities, we hereinafter consider only real nonnegative solutions.

Fixed points: In order to investigate the solutions of system, we start by examining the case where $\alpha < \alpha_0$. Clearly, the unique solution is $E_1 = (0, 0, 0, 0, 0)$.

As for $\alpha > \alpha_0$, we proceed as follows:

Equation leads to two different solutions: $C_3 = 0$ or $C_3 = \frac{\lambda 5}{d3} M_1 - k_3$.

We notice that solving equations and for $C_3 = 0$ is equivalent to solve

$$d_1 L_{ox}^2 + (d_1 k_1 - \lambda_1) L_{ox} = 0.$$ Eq.(2.39)

The latter equation admits two solutions

$$L_{ox_0} = \frac{\lambda_1 - d_1 k_1 - \sqrt{(\lambda_1 - d_1 k_1)^2}}{2d_1} \text{ and } L_{ox_1} = \frac{\lambda_1 - d_1 k_1 + \sqrt{(\lambda_1 - d_1 k_1)^2}}{2d_1}$$ Eq.(2.40)

Therefore, in the hyperplane $C_3 = 0$, there exists two fixed points E_0 and E_1 having the following components:
If $\lambda_1 < d_1 k_1$
If $\lambda_1 > d_1 k_1$

$$E_0 = \left(\frac{\lambda_1}{k_L} \frac{L_{ox_0}}{k_1 + L_{ox_0}}, L_{ox_0}, \frac{\lambda_3}{\lambda_4} \frac{L_{ox_0}}{k_1 + L_{ox_0}}, \frac{d_1 \lambda_3}{d_2 \lambda_1} L_{ox_0}, 0 \right)$$

$$= \begin{cases} \left(\frac{\lambda_1 - d_1 k_1}{k_L}, \frac{\lambda_1 - d_1 k_1}{d_1}, \frac{\lambda_3}{\lambda_4} \frac{\lambda_1 - d_1 k_1}{\lambda_1}, \frac{\lambda_3}{d_2 \lambda_1} (\lambda_1 - d_1 k_1), 0 \right) \\ (0, 0, 0, 0, 0) \end{cases}$$ Eq.(2.41)

If $\lambda_1 < d_1 k_1$
If $\lambda_1 > d_1 k_1$

$$E_1 = \left(\frac{\lambda_1}{k_L} \frac{L_{ox_1}}{k_1 + L_{ox_1}}, L_{ox_1}, \frac{\lambda_3}{\lambda_4} \frac{L_{ox_1}}{k_1 + L_{ox_1}}, \frac{d_1 \lambda_3}{d_2 \lambda_1} L_{ox_1}, 0 \right)$$

$$= \begin{cases} (0,0,0,0,0) \\ \left(\frac{\lambda_1 - d_1 k_1}{k_L}, \frac{\lambda_1 - d_1 k_1}{d_1}, \frac{\lambda_3}{\lambda_4} \frac{\lambda_1 - d_1 k_1}{\lambda_1}, \frac{\lambda_3}{d_2 \lambda_1}(\lambda_1 - d_1 k_1), 0 \right) \end{cases}$$

Eq.(2.42)

In a similar manner, we proceed in the plane $C_3 = \frac{\lambda 5}{d3} M_1 - k_3$. The L_{ox} component of the fixed points in this plane verify the following equation, that is obtained from equations:

$$- d_1 \left(1 + \frac{d_1 \lambda_3 \lambda_5}{d_2 d_3 \lambda_1} \right) L_{ox}^2 + \left(\lambda_1 \left(1 + \frac{d_1 \lambda_3 \lambda_5}{d_2 d_3 \lambda_1} \right) - d_1 (k_1 - k_3) \right) L_{ox} - k_3 \lambda_1 = 0.$$

Eq.(2.43)

Equations admits two solutions:

$$L_{ox_u} = \frac{\lambda_1 \left(1 + \frac{d_1 \lambda_3 \lambda_5}{d_2 d_3 \lambda_1} \right) - d_1 (k_1 - k_3) - \sqrt{\left(\lambda_1 \left(1 + \frac{d_1 \lambda_3 \lambda_5}{d_2 d_3 \lambda_1} \right) - d_1 (k_1 - k_3) \right)^2 - 4 d_1 k_3 \lambda_1 \left(1 + \frac{d_1 \lambda_3 \lambda_5}{d_2 d_3 \lambda_1} \right)}}{2 d_1 \left(1 + \frac{d_1 \lambda_3 \lambda_5}{d_2 d_3 \lambda_1} \right)}$$

Eq.(2.44)

$$L_{ox_2} = \frac{\lambda_1 \left(1 + \frac{d_1 \lambda_3 \lambda_5}{d_2 d_3 \lambda_1} \right) - d_1 (k_1 - k_3) + \sqrt{\left(\lambda_1 \left(1 + \frac{d_1 \lambda_3 \lambda_5}{d_2 d_3 \lambda_1} \right) - d_1 (k_1 - k_3) \right)^2 - 4 d_1 k_3 \lambda_1 \left(1 + \frac{d_1 \lambda_3 \lambda_5}{d_2 d_3 \lambda_1} \right)}}{2 d_1 \left(1 + \frac{d_1 \lambda_3 \lambda_5}{d_2 d_3 \lambda_1} \right)}.$$

Eq.(2.45)

Upon that, we consider the following inequalities:

-Condition A:

$$\lambda_1 \left(1 + \frac{d_1 \lambda_3 \lambda_5}{d_2 d_3 \lambda_1} \right) - d_1 (k_1 - k_3) > 0.$$

Eq.(2.46)

-Condition B:

$$\left(\lambda_1 \left(1 + \frac{d_1 \lambda_3 \lambda_5}{d_2 d_3 \lambda_1} \right) - d_1 (k_1 - k_3) \right)^2 - 4 d_1 k_3 \lambda_1 \left(1 + \frac{d_1 \lambda_3 \lambda_5}{d_2 d_3 \lambda_1} \right) > 0.$$

Eq.(2.47)

-Condition C:

$$\frac{d_1\lambda_3\lambda_5}{d_2 d_3 \lambda_1} L_{ox_2} - k_3 > 0.$$

For simplicity, when conditions A and B are satisfied and $k_1 < k_3$, we assume that:

$$-\lambda_1\left(1+\frac{d_1\lambda_3\lambda_5}{d_2 d_3 \lambda_1}\right)-d_1(k_1-k_3)+\sqrt{\left(\lambda_1\left(1+\frac{d_1\lambda_3\lambda_5}{d_2 d_3 \lambda_1}\right)-d_1(k_1-k_3)\right)^2-4d_1 k_3 \lambda_1\left(1+\frac{d_1\lambda_3\lambda_5}{d_2 d_3 \lambda_1}\right)} < 0.$$

In case that conditions A, B and C are verified, there exists two fixed points E_u and E_2 in the plane $C_3 = \frac{\lambda 4}{d3} M_1 - k_3$, where:[8]

$$C_3 = \frac{\lambda_4}{d_3} M_1 - k_3, \text{ where:}$$

$$E_2 = \left(\frac{\lambda_1}{k_L}\frac{L_{ox_2}+\frac{d_1\lambda_3\lambda_5}{d_2 d_3 \lambda_1}L_{ox_2}-k_3}{k_1+L_{ox_2}+\frac{d_1\lambda_3\lambda_5}{d_2 d_3 \lambda_1}L_{ox_2}-k_3}, L_{ox_2}, \frac{\lambda_3}{\lambda_4}\frac{L_{ox_2}+\frac{d_1\lambda_3\lambda_5}{d_2 d_3 \lambda_1}L_{ox_2}-k_3}{k_1+L_{ox_2}+\frac{d_1\lambda_3\lambda_5}{d_2 d_3 \lambda_1}L_{ox_2}-k_3}, \frac{d_1\lambda_3}{d_2\lambda_1}L_{ox_2}, \frac{d_1\lambda_3\lambda_5}{d_2 d_3 \lambda_1}L_{ox_2}-k_3\right).$$

And

$$E_u = \left(\frac{\lambda_1}{k_L}\frac{L_{ox_u}+\frac{d_1\lambda_3\lambda_5}{d_2 d_3 \lambda_1}L_{ox_u}-k_3}{k_1+L_{ox_u}+\frac{d_1\lambda_3\lambda_5}{d_2 d_3 \lambda_1}L_{ox_u}-k_3}, L_{ox_u}, \frac{\lambda_3}{\lambda_4}\frac{L_{ox_u}+\frac{d_1\lambda_3\lambda_5}{d_2 d_3 \lambda_1}L_{ox_u}-k_3}{k_1+L_{ox_u}+\frac{d_1\lambda_3\lambda_5}{d_2 d_3 \lambda_1}L_{ox_u}-k_3}, \frac{d_1\lambda_3}{d_2\lambda_1}L_{ox_u}, \frac{d_1\lambda_3\lambda_5}{d_2 d_3 \lambda_1}L_{ox_u}-k_3\right),$$

2.2 Conclusion

This work is devoted to the mathematical modeling of atherosclerosis. It provides an initial model that describes the anti and pro-inflammatory processes arising during the atherogenesis through partial differential equations of reaction-diffusion type. The endothelial functionality is examined and integrated to the model. A reduced model considering the pro-inflammatory process is then derived from the complete model and analyzed. It shows that the initiation of the inflammation is determined by the endothelial function and the penetration of LDL within the intima. Besides, experimental data reported from the literature contribute to providing a diagram of risk zones according to the values of two critical parameters. Likewise, numerical simulations emphasize the existence of traveling wave solutions for the reduced monotone model. The existence of perturbed solutions and perturbed traveling wave solutions are also investigated. Then the transition from reduced model to the complete initial model is studied along with graphical results. A conformity in results between the reduced and complete model is perceived for a certain range of parameters. Bifurcation diagrams show the evolution of the inflammation depending on endothelial permeability and LDL penetration to the intima. The analysis of the complete model simulations reveals a regulation of the inflammation development due to the integration of the anti-inflammatory cascades. Even though the conclusions approve and generalize previous results, this model has some limitations. In this model many assumptions were imposed. Some of them are related to the monotonicity of the reduced model. To overcome these conditions we proved the existence of perturbed solutions. It signifies that a high endothelial permeability is associated with a high release of pro-inflammatory cytokines. From a biological point of view, this assumption is commonly valid since endothelial dysfunction promotes endothelial activation and consequently the release of pro-inflammatory cytokines. However, due to some pathologic issues, this relationship between endothelial permeability and pro-inflammatory cytokines can be altered. More details on dependance of pro-

inflammatory cytokines on endothelial dysfunction are beneficial to provide a more detailed classification. The domain of this model is one-dimensional. A more accurate representation for complex conditions can be done by considering 2D and 3D models, where the artery can be represented by a rectangular or cylindrical domain, the study infers on intimal accumulation of cholesterol and plaque formation. Moreover, a fluid-structure interaction study can describe interactions between blood dynamics and the structural mechanics of the arterial wall. Since the blood's behavior is greatly affected by the deformation of the artery, the mechanical analyses are used to provide rigorous representations of flow distribution and explore possible plaque rupture mechanisms.

Chapter Three

3.1 Introduction

In the chapter background Alzheimer disease (AD) is a progressive neurodegenerative disease that destroys memory and cognitive skills. AD is characterized by the presence of two types of neuropathological hallmarks: extracellular plaques consisting of amyloid β-peptides and intracellular neurofibrillary tangles of hyperphosphorylated tau proteins. The disease affects 5 million people in the United States and 44 million world-wide. Currently there is no drug that can cure, stop or even slow the progression of the disease. If no cure is found, by 2050 the number of alzheimer's patients in the U.S. will reach 15 million and the cost of caring for them will exceed $ 1 trillion annually.[13](Davodabadi, Afsaneh, et al. "Mathematical model and artificial intelligence for diagnosis of Alzheimer's disease." The European Physical Journal Plus 138.5 (2023): 474.)

3.1.1 The use of mathematical modeling in the treatment of Alzheimer's disease

research has shown that such facial expressions may be utilized as a significant indicator in the diagnosis of mental health issues such schizophrenia, depression, autism, and bipolar disorder, among others. An unhealthy relationship with unpleasant emotions, an inability to express feelings, or emotional instability have all been linked to the aforementioned disorders.[20] Human analysis in picture analysis is an intriguing problem in machine vision.[21][22] Human computer interaction, emotion analysis, interactive video, display and retrieval from picture and video databases, and computer-generated face animation are just some of the many applications of face recognition technology. The human face may be utilized to convey non-verbal and conceptual information to a computer, including a person's emotional and spiritual state.[23](Davodabadi, Afsaneh, et al. "Mathematical model and artificial intelligence for diagnosis of Alzheimer's disease." The European Physical Journal Plus 138.5 (2023): 474.)

Figure (2.1) Memory loss and inability to recognize objects (Alzheimer's)

3.1.2 Fractal feature extraction

In order to extract features, it is necessary to streamline the techniques used to narrowly define a large dataset.[14] The fractal model is used to generate the characteristic in this investigation. The collection of characteristics was used to reduce the feature size and to determine the most crucial traits for making accurate category distinctions.[15] The dimensionality reduction and Eigenvalue generation in the picture were accomplished with the help of covariance analysis and the fractal technique. In the fractal algorithm, the input vectors need to have the same size and have a representation described as a 2-dimensional matrix. There is a hard requirement that high-resolution photos be grayscale.

The objects are assembled using an M × N matrix, where M is the number of objects in each picture and N is the number of points in each image. And M stands for the overall size of the picture database. The average picture must be measured in order tocompute an standard deviation from any major input matrix. From there, we may calculate the covariance matrix and its eigenvalues and eigenvectors. In the fractal algorithm, M indicates the number of instructional images. And Fi will show the images average and li will indicate each Ti vector image. There are initially M images, each of which contains the N × N dimension. An N-dimensional space can exhibit each

image, which is computed as Eqs. (2.1) and (2.2) indicates averaging operation.[16]

$$A = N \times N \times M \qquad \text{Eq.(2.1)}$$

$$F_{i=}\frac{1}{M}\sum_{t=1}^{m} T_t \qquad \text{Eq.(2.2)}$$

A huge problem in the fractal techniques determined by Eq. (2.3) and the covariance matrix of Eq. (2.4) is called the specification of the standard deviation.

$$\text{Variance} = \frac{1}{N}\sum(x - \mu) \qquad \text{Eq.(2.3)}$$

$$Cov = AA^T \qquad \text{Eq.(2.4)}$$

where $A = [V\,ariance_1, V\,ariance_2, ..., V\,ariance_n]$ and $Cov = N^2 \times N^2$ and $A = N^2 \times M$. Therefore, Cov is large value that eigenvalues of Cov are evaluated by Equation (2.5).

$$U_i = AV_i \qquad \text{Eq.(2.5)}$$

The final step is choosing a vector with Eigen. A sequence of properties of a state-inherent function as N ($N = 213$) in $\{x_1, x_2, ...,x_N\}$ belonging to the C ($C = 7$).

The class can be found on $\{L_i \,|i = 1, 2, ..., C\}$. The fractal method aims to map data to f-dimension space that $f < d$. At $y_i = R^f$ the new vector feature is placed. Scattered class matrices are covariance tables measured by Eq.(2.6) and Eq.(2.7)

$$S_T = \sum_{k=1}^{N}(x_k - \mu)(x_k - \mu)^T \qquad \text{Eq.(2.6)}$$

$$W_{\text{Fractal}} = \arg\max[W^T S_T W] = [w_1 w_2...w_f] \qquad \text{Eq.(2.7)}$$

where the value for all the samples is μ and $\{w_i \,|i = 1, 2, ..., f\}$ is a set of the eigenvector of f-dimension of S_T that is associated with the largest eigenvalue f. Samples in the new space are $y = W^T x$, which is $W_{Fractal} \in R^{f \times xd}$ ($170 \times d$).[16]

(Davodabadi, Afsaneh, et al. "Mathematical model and artificial intelligence for diagnosis of Alzheimer's disease." The European Physical Journal Plus 138.5 (2023): 474.)

3.1.3 Concept of deep convolutional neural network

One of the most important deep learning methods is the convolutional neural network. Primary convolutional layers, maxpooling lay- ers, fully connected layers, and additional layers implementing different characteristics are

common components of a convolutional neural network. Each system's preparation consists of two stages: forward and reverse progression.[17]

The process begins with information entering the input layer, continuing through the concealed layer, and finally exiting the output layer. The initial phase of the backpropagation technique is for the input picture to feed the network. At the completion of the process, the error value is calculated. As well as changing the network weight and the cost functions diagram, this value is then sent back into the network see Figure (2.2). The hidden sub-layers that make up a CNN are of several sorts, as can be shown in the following discussion:[17]

The foundation of every convolutional network is the convolutional layer. The output of this layer is a three-dimensional neuron matrix. Convolutional neural network transformation of input picture and central function mappings need various kernels in certain layers. There are three significant benefits to the convolution procedure:

- The number of nodes in each function diagram is reduced using the weight-sharing approach. Since the local link between neighboring pixels is known, the target's location may be adjusted to achieve a state of equilibrium.
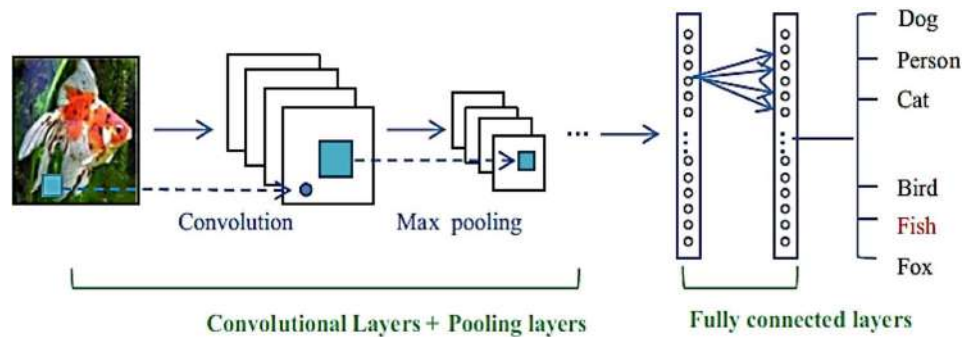
Figure (2.2) A description of a CNN architecture
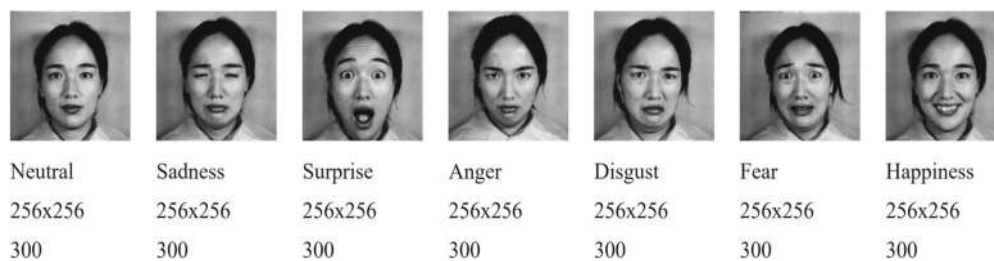
Figure (2.3) Images samples in JEFFE dataset: images size is 256×256 grayscale image in tiff format
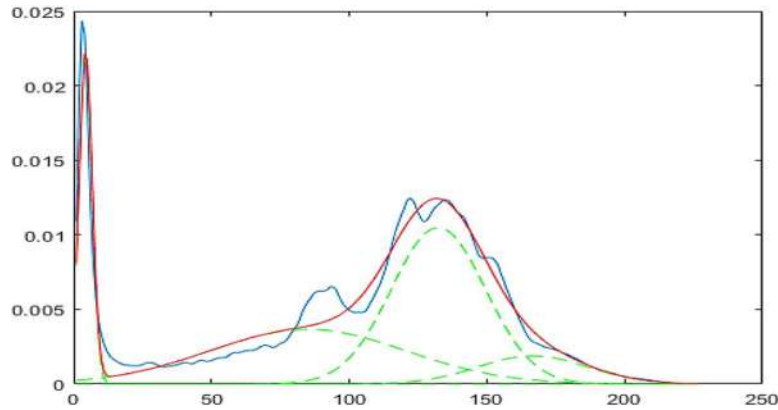
Figure (2.4) Feature extraction process over a plot of the fractal model

- Activation functions are a key component of neural networks, and are responsible for producing the desired results. There are many other activation functions that may be used in neural networks, but the two most important are the Tanh and the Sigmoid. Input data $(-- +)$ are transformed by the sigmoid function into the range $[0, 1]$. Tanh data ranges from -1 in terms of production value. Recently, the ReLU function has been presented as an alternative activation function. ReLU is a generalized activation function. The goal is to challenge the network in a way that is not linear. Using this feature, every negative pixel value is changed to zero (64).

- Max pooling: The usage of Maxpooling in CNN has a number of repercussions. By using it, CNN may first specify the goal with little changes to the matrix. Second, the large scale of the picture aids CNN in identifying characteristics. CNN Maxpooling is utilized to perform a subtraction-based summation of the function during the sampling phase, allowing for access to intermediate and advanced levels of CNN. If we want to keep this knowledge, we will need to start sharing what we have. The two most typical types of pooling are the Maximum and the Average.

Data preparation, preprocessing, and data improvement are among the most underappreciated challenges. This step, however, isn't usually required. You should determine whether your work requires pre-processing before beginning any kind of data processing.[17])(Davodabadi, Afsaneh, et al. "Mathematical model and artificial intelligence for diagnosis of Alzheimer's disease." The European Physical Journal Plus 138.5 (2023): 474.)

3.1.4 Support vector machine

Suppose we have the set of data points $\{(x_1, c_1), (x_2, c_2), ..., (x_n, c_n)\}$., And we want to classify them into two classes $c_i = \{1, -1\}$. Each x_i is a p-dimensional vector of R that is the features. For data separation between two classes, the

SVM classification algorithm identifies optimal hyperparameters. The key is to choose the appropriate delimiter. The most distant divider between the
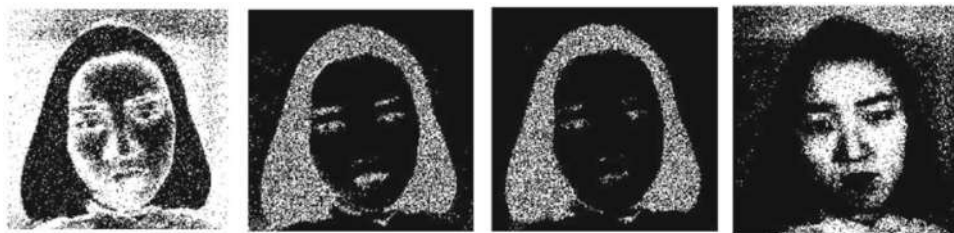

Figure (2.5) Fractal extracted functions in the form of the main image matrix

Figure (2.6) Confusion matrix of training data using SVM method

	Polynomial		RBF		Linear	
	Train	Test	Train	Test	Train	Test
Accuracy	69.20	68. 63	89.83	94.29	56.34	82.34
Specificity	83.03	79.38	89.22	86.51	49.57	68.58
Sensitivity	13.12	18.54	67.83	71.93	23.69	22.44
F1 score	15.63	9.55	62.22	58.89	22.19	10.12
Gmeans	23.85	26.37	73.63	69.12	29.27	27.49

Table (2.1)Results of performance analyasis

two groups is the one being discussed. Its boundary points span not one but two classes, making it the most comprehensive.[18] The mathematical formulas of these two parallel hyperparameters that make up the separator boundary are shown in Eq.(2.7) and (2.8):

$wx - b = 1.$ Eq. (2.8)
$wx - b = -1$ Eq. (2.9)

If the training data are linearly separable, then the distance between the two

parallel hyperparameters may be maximized by choosin the two border hyperparameters in such a manner that there is no data between them. Using geometric theorems, the distance between these two hyperparameters is $\frac{2}{|w|}$, So $|w|$ should minimized. In addition, a mathematical constraint must be added to the formal specification to ensure that no data points are ever brought inside the border. For each i, the following constraints are applied to ensure that no point is placed on the boundary:

First class: $wx_i - b \geq 1$ Eq.(2.10)

Second class: $wx_i - b \leq -1$ Eq.(2.11)

The following equations can be shown as follows:

$c_i(wx_i - b) \geq 1, 1 \leq i \leq n$ Eq.(2.12)

Therefore, the optimization problem is defined with minimizing w, taking into account the Eq. (2.12) limitations.[19](Davodabadi, Afsaneh, et al. "Mathematical model and artificial intelligence for diagnosis of Alzheimer's disease." The European Physical Journal Plus 138.5 (2023): 474)

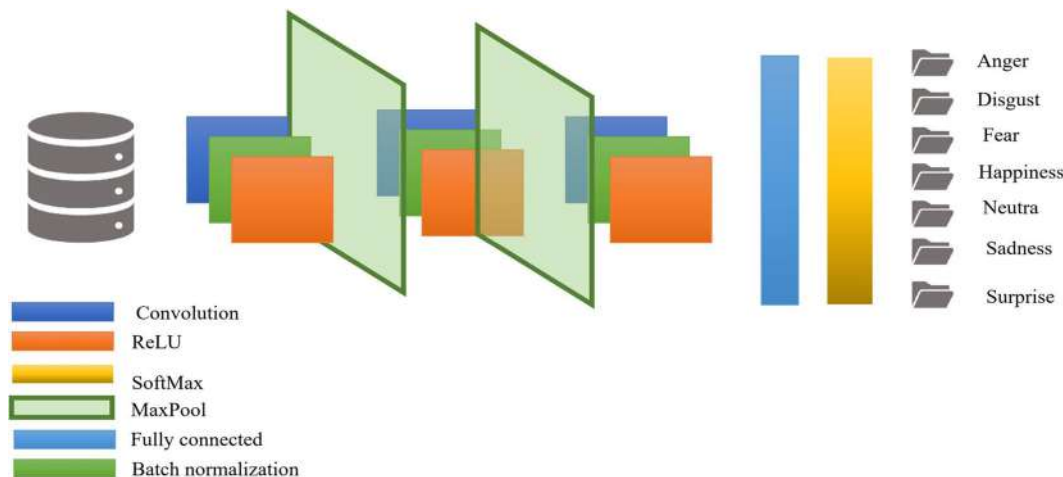Figure (2.7) Confusion matrix of testing data using SVM method

Figure (2.8) The presented DCNN architecture

3.1.5 Performance analysis

Accuracy, Re-call or sensitivity, Specificity, F1-score, and geometric mean sensitivity and specificity (Gmeans) are used in this analysis to determine the effects of the classification. A system ability to discover new patients is measured by its Recall and accuracy rate. Each class overall performance, including classification accuracy and recall, is measured using the F1. This section defines these standards.[12]

$$\text{Accuracy} = \frac{TP+TN}{TP+FP+FN+T} \qquad \text{Eq.(2.13)}$$

$$\text{Precision} = \frac{TP}{TP+FP} \qquad \text{Eq.(2.14)}$$

$$\text{Recall} = \frac{TP+T}{TP+TN} \qquad \text{Eq.(2.15)}$$

$$\text{Specificity} = \frac{TN}{FP+T} \qquad \text{Eq.(2.16)}$$

| Layer	Name	Description
1	Image input	256×256×1 images with 'zero center' normalization
2	Convolution	8(3×3) convolutions with stride [1 1] and padding 'same'
3	Batch normalization	Normalization
4	ReLU	Rectifier
5	Pooling	2×2 max pooling with stride [2 2] and padding [0 0 0 0]
6	Convolution	16(3×3) convolutions with stride [1 1] and padding 'same'
7	Batch normalization	Normalization
8	ReLU	Rectifier
9	Pooling	2×2 max pooling with stride [2 2] and padding [0 0 0 0]
10	Convolution	32(3×3) convolutions with stride [1 1] and padding 'same'
11	Batch normalization	Normalization
12	ReLU	Rectifier
13	Fully connected	7 fully connected layer
14	SoftMax	SoftMax
15	Classification output	Cross entropy

Table (2.2) The presented DCNN architecture layers
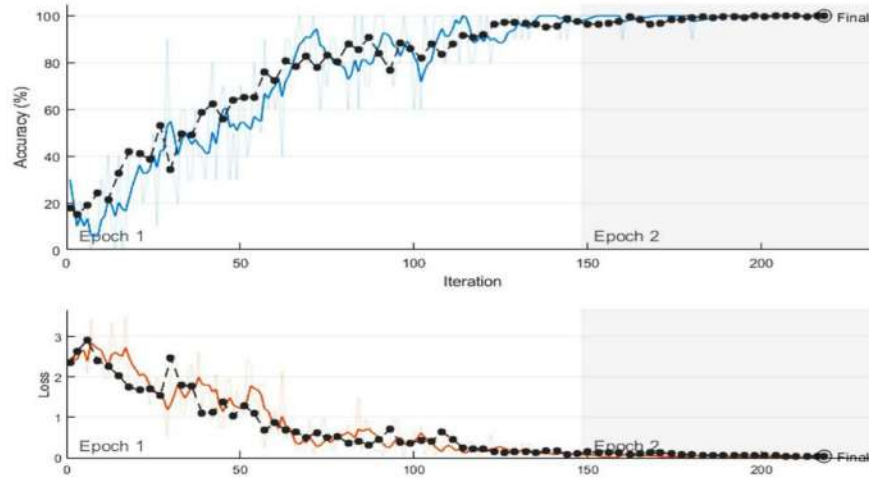
Figure (2.9) DCNN training process: accuracy and loss value for 300 iteration

$$\text{Sensitivity} = \frac{\text{TP}}{\text{TP+F}} \qquad \text{Eq.(2.17)}$$

$$\text{F1score} = 2\frac{\text{Precision×Recall}}{\text{Precision×Rec}} \qquad \text{Eq.(2.18)}$$

$$\text{Gmeans} = \sqrt{\text{Specificity} \times \text{Sensitivity}} \qquad \text{Eq.(2.19)}$$

The performance matrix helps to characterize the efficiency of the classification model on several categorized datasets.

Figure (2.10) The results of the confusion matrix for training data of DCNN

3.2 Results and discussion

3.2.1 Data collection

There are a total of 213 photos in the Japanese Female Facial Expression (JAFFE) collection, depicting 7 different emotions (6 different expressions + 1 neutral expression). The models for these photographs are 10 different women from Japan. Sixty Japanese individuals rate each picture on six different emotional scales. Three people, Michael Lyons, Miyuki Kamachi, and Jiro Gyoba, are responsible for the creation and compilation of this database. Several scientific studies have made use of JAFFE pictures. Gray scale photos at a resolution of 256 × 256 are provided in uncompressed.tiff format.[12]

The main dataset contains 213 images so in this paper for increasing accuracy and preventing possible overfitting we used dataaugmentation techniques with some filters, histogram, and adding noise to the image to increase dataset size. Therefore, each mental state includes 300 images. Data set volume augmented to 2100 images.[12] (Davodabadi, Afsaneh, et al. "Mathematical model and artificial intelligence for diagnosis of Alzheimer's disease." The European Physical Journal Plus 138.5 (2023): 474.)

3.2.2 Feature extraction using the fractal model

An example of a feature extraction diagram for one of the photos is shown in Figure (2.4). The frequency distribution of the image pixels is shown by the blue histogram in Fig. 4. Finding the optimal normal functions for modeling the histogram is the focus of the fractal approach. From this, we may estimate the image histogram with a sum of three red functions, each of which is represented by a green Gaussian function. Coefficients of standard green functions are equivalent to those of the resulting images in terms of their attributes. In light of this, we have catalogued four characteristics for every picture. If we can use these four operations to create the primary picture, it will look like Figure (2.5).[12] (Davodabadi, Afsaneh, et al. "Mathematical model and artificial intelligence for diagnosis of Alzheimer's disease." The European Physical Journal Plus 138.5 (2023): 474.)

3.2.3 Implementation of classification using SVM kernels

In this subsection, facial expressions are identified using the support vector machine (SVM) technique. In this case, the JAFFE dataset was mined for information. Three hundred face photographs were assessed for each scenario, for a total of 2100 image.[12]

Figure (2.11) The results of the confusion matrix for testing data of DCNN

analyzed (75 % for model training and 25 % for testing and verification). Each of the seven emotions (anger, disgust, fear, happiness, neutral, sadness, and surprise) were represented by one of seven possible labels (1–7), with each image having four features as independent variables.

Different kernels were also employed to training the model and the outcomes have been compared. The following are the outcomes of the classification using a polynomial kernel of degree 5. Figure (2.6) illustrates the confusion matrix in training data. In this picture, the diagonal diameters show the number of accurate classifications by the trained network. Table (2.1) provides the results of the performance assessment criteria for the suggested technique.[12]

Now we will evaluate the SVM method various kernels side by side. Table (2.1) summarizes the outcomes of using polynomial kernels, radial basis functions (RBFs), and linear kernels for this purpose. The training data comparison table shows that the polynomial approach with order 5 meets the most requirements. The findings show that the RBF model's SVM accuracy is 93.18 percent for the training data and 89.33 percent for the

testing data. The RBF kernel has stricter performance requirements than competing techniques. It has a 96 % sensitivity for diagnosing a mental state, but only an 86.67 % sensitivity for a Linear kernel and an 86.03% sensitivity for a polynomial kernel Figure (2.7). (Davodabadi, Afsaneh, et al. "Mathematical model and artificial intelligence for diagnosis of Alzheimer's disease." The European Physical Journal Plus 138.5 (2023): 474.)

3.2.4 Implementation of classification using DCNN

We will use a deep convolution neural network to analyze facial expressions and label them accordingly. The approach presented for the deep convolutional network algorithm as according Figure (2.8) consists of five layers, which are: Human face photos from the JAFFE collection, which comprises 2100 images in 7 Face mode (6 face modes + 1 neutral) from 10 Japanese female models. An picture of size 256x256 with 7 face modes is used to create a 4D matrix of size 2100 by 2100 in this layer.

Convolution occurs in the second layer, and it employs 8(3 × 3) filters to iteratively process the input matrix. In this research, the convolution matrix is constructed by adding a border of zeros to the input matrices. The array is analyzed in one pass by the filter as well. Matrix transformation is used in the third layer of normalization. The ReLU function, often seen in convolution networks, is used in the activation function layer, the fourth layer of a convolution network. After each layer of convolution, this function clears the matrix of any negative values and passes on its positive values to the subsequent layer. Pooling occurs on the sixth layer. This layer is a sampling technique for a convolutional neural network that functions on the pixel space and is capable of maximizing within the filter range. These subsequent levels are organized into three distinct classes. Figure (2.8) and Table (2.2) show that a completely linked layer does not appear until the thirteenth iteration. When this layer is applied on top of a matrix, the result is a vector that may be evaluated by the output layer. If you want to be technical, it creates 7 submatrices (number of categories). The SoftMax layer, located at position 14, is the last output layer of a multi-layer classification neural network. The SoftMax function takes in values from a number of different rankings and outputs a single value between zero and one that is the total of all the

ranks. To quantify the degree of inaccuracy associated with a given value of the dependent variable, the classification layer is used as the study's output layer. This layer influences when we come closer to the most accurate result. The MSE criteria, or average squared error, is utilized here. The repeat loop runs until it obtains the desired outcome. Finally, the output is identified by 7 labels with the names of the face expressions that decide the result.The RMSE error generated by the DCNN software is shown in Figure (2.9). There were two epochs, each with 150 periods, and 300 iterations in all. On the test set, which comprises 30 % of the whole data set, the ultimate accuracy of this study is 0.99. In addition, the final iteration has nearly little data loss.

In this study, we evaluate the computational endpoint based on the convergence slope, which must be horizontal (zero) in Figure (2.9) errors and losses perspective. The training data confusion matrix is shown in Figure (2.10). The figure's diagonal diameters represent the percentage of instances when the trained network correctly classified the data. Example: all 300 photos were accurately labeled as depicting rage. All the photos have been properly detected and trained, i.e. with a hundred percent accuracy and sensitivity, thanks to the confusion matrix of training data. Nonetheless, the test sample confusion matrix is shown in Figure (2.10). Diagnostic accuracy is close to perfect, with the lowest rate being for depression. Only one out of ninety randomly chosen photographs is incorrectly categorized as cheerful. Consequently, we can say with 99.8 percent certainty that the tests have been accurate.(Davodabadi, Afsaneh, et al. "Mathematical model and artificial intelligence for diagnosis of Alzheimer's disease." The European Physical Journal Plus 138.5 (2023): 474.)

3.3 Conclusion

In this work, we explore how a smart environment may automatically make use of pictures and emotions to improve healthcare. To tailor our care to each patient, we utilized visual cues to determine how they were feeling. To do this, we employed the Support vector machine for classification after extracting fractal characteristics from the photos. There have been experiments done in this area, and it has been possible to accurately identify each mental state one hundred percent of the time. Good convergence was obtained using the suggested DCNN model, and the accuracy of the test data was close to 98%. Patients' mental health may also be assessed using the support vector machine technique. The JAFFE was mined for information. Two hundred and ten facial photos were assessed for each scenario, with seventy-five percent used for model training and twenty-five percent for testing and verification. Anger, disgust, fear, happiness, neutral, sorrow, and surprise labels (1–7) were used to categorize each picture, with each of the four fractal aspects serving as an independent variable. In the end, the SVM approach was accurate enough to accurately identify around 93% of the photos tested. When it came to training models, DCNN was 97.8% accurate, whereas SVM was only 93% accurate. Comparing DCNN with SVM, the latter's test results accuracy was 89.33% while the former's was 98.8%. Psychologists assert that one's emotions play a key part in providing care to patients. Therefore, we adopted a method to verify the whole idea with regards to efficacy, accuracy, and statistical analysis, considering these characteristics and experiments. For the sake of making headway in the treatment of illnesses like Parkinson's and Alzheimer's, we want to leverage evolutionary principles in our future research to develop facial expression categorization algorithms. Alzheimer's disease does not completely alter the facial appearance of its sufferers. Since our model requires processing and communication cycles in addition to evolutionary techniques, this might be a good challenge once again when applied to a diverse situation. Furthermore, we want to improve our approach to emotion identification by considering many angles of the face, the expression, and the posture.[12]

REFERENCES

1. ASHRAFIAN, Hutan. Mathematics in medicine: the 300-year legacy of iatromathematics. Lancet, 382.9907: 1780, 2013.

2. GUERRINI, Anita. Archibald Pitcairne and Newtonian Medicine. Medical history, 31.1: 70-83, 1987.

3. ASHRAFIAN, Hutan. Leonardo da Vinci's Vitruvian Man: a renaissance for inguinal hernias. Hernia, 15.5: 593-594, 2011.

4. ASHRAFIAN, Hutan; HARLING, Leanne; ATHANASIOU, Thanos. Leonardo da Vinci and the first portrayal of quadricuspid semilunar valves and the nodules of Arantius. International journal of cardiology, 165.3: 560-561, 2013.

5. COCKCROFT, James, et al. Why Do We Need Maths in Medicine?. Frontiers for Young Minds, 9, 2021.

6. BUDD, Chris; MITCHELL, Cathryn. Saving lives: the mathematics of tomography. Plus Magazine, 47, 2008.

7. Kalender, Willi A. Computed tomography: fundamentals, system technology, image quality, applications. John Wiley & Sons, 2011.

8. ABI YOUNES, Ghada; EL KHATIB, Nader. Mathematical modeling of inflammatory processes of atherosclerosis. Mathematical Modelling of Natural Phenomena, 17: 5, 2022.

9. Epstein, Charles L., ed. Introduction to the mathematics of medical imaging. Society for Industrial and Applied Mathematics, 2007.

10. Kuchment, Peter, et al. "Mathematical Methods of Computed Tomography",2012.

11. DAVODABADI, Afsaneh, et al. Mathematical model and artificial intelligence for diagnosis of Alzheimer's disease. The European Physical Journal Plus, 138.5: 474, 2023.

12. YU, Kun-Hsing; BEAM, Andrew L.; KOHANE, Isaac S. Artificial intelligence in healthcare. Nature biomedical engineering, 2.10: 719-731, 2018.

13. HAN, Dongying; ZHAO, Na; SHI, Peiming. Gear fault feature extraction and diagnosis method under different load excitation based on EMD, PSO-SVM and fractal box dimension. Journal of Mechanical Science and Technology, 33: 487-494, 2019.

14. SRINIVASAN, A., et al. Brain MR image analysis using discrete wavelet transform with fractal feature analysis. In: 2018 Second International Conference on

Electronics, Communication and Aerospace Technology (ICECA). IEEE. p. 1660-1664, 2018.

15. CHAURASIA, Vijayshri; CHAURASIA, Vaishali. Statistical feature extraction based technique for fast fractal image compression. Journal of Visual Communication and Image Representation, 41: 87-95, 2016.

16. MCCANN, Michael T.; JIN, Kyong Hwan; UNSER, Michael. Convolutional neural networks for inverse problems in imaging: A review. IEEE Signal Processing Magazine, 34.6: 85-95, 2017.

17. LAND JR, Walker H., et al. The support vector machine. The Art and Science of Machine Intelligence: With An Innovative Application for Alzheimer's Detection from Speech, 45-76, 2020.

18. SUTHAHARAN, Shan. Machine learning models and algorithms for big data classification. Integr. Ser. Inf. Syst, 36: 1-12, 2016.

19. KESSELS, Roy PC, et al. Assessment of perception of morphed facial expressions using the Emotion Recognition Task: Normative data from healthy participants aged 8–75. Journal of neuropsychology, 8.1: 75-93, 2014.

20. DAROS, Alexander R., et al. Facial emotion recognition in first-episode schizophrenia and bipolar disorder with psychosis. Schizophrenia research, 153.1-3: 32-37, 2014.

21. BREWER, Rebecca, et al. Can neurotypical individuals read autistic facial expressions? Atypical production of emotional facial expressions in autism spectrum disorders. Autism Research, 9.2: 262-271, 2016.

22. KELTNER, Dacher, et al. Emotional expression: Advances in basic emotion theory. Journal of nonverbal behavior, 43: 133-160, 2019.

الخلاصة

"في هذا البحث، تُعرض أهمية الرياضيات في الطب. يتم استخدام العديد من أدوات الرياضيات مثل موضوع المصفوفات، بالإضافة إلى زوايا المثلث، بما في ذلك ١٨٠ درجة و٣٠ درجة و٤٥ درجة في تشغيل جهاز التصوير المقطعي وجهاز التصوير بالرنين المغناطيسي (MRI). كما يُعطى مثال على شخص يعاني من الصداع ويريد معرفة كيفية عمل جهاز MRI باستخدام المصفوفات. علاوة على ذلك، يُناقش موضوع رياضي آخر وهو المعادلات التفاضلية في الكشف والعلاج المبكر لتصلب الشرايين. حيث تم تحويل الأعراض والعلاجات إلى معادلات تفاضلية وتم حلها. أيضًا، يُناقش مرض الزهايمر (AD) وهو مرض عصبي تنكسي تدريجي يدمر الذاكرة والمهارات المعرفية. تم تحديد العديد من خصائص هذا المرض مثل: كيفية استخدام النمذجة الرياضية في علاج مرض الزهايمر؟، استخراج السمات الكسورية، مفهوم شبكة العصبونات العميقة التلافيفية، آلة الدعم الناقل، وتحليل الأداء. وأخيرًا، يتم مناقشة النتائج المهمة لجمع البيانات، استخراج السمات باستخدام النموذج الكسوري، تنفيذ التصنيف باستخدام أنوية SVM ، وتنفيذ التصنيف باستخدام DCNN."

جمهورية العراق.

وزارة التعليم العالي و البحث العلمي.

جامعة بابل.

كلية التربية للعلوم الصرفة.

بعض التطبيقات الرياضية في الطب

بحث مقدم إلى جامعة بابل / كلية التربية للعلوم الصرفة / قسم الرياضيات كجزء من متطلبات درجة البكالوريوس في العلوم الرياضية

من قبل

ريام اياد جبر

المشرف على البحث

أ.م.د. أحمد عبد علي